

AFRC Industrial Combustion Symposium
October 10-12, 2021
Houston, TX

A Bayesian Approach to Quantifying the Uncertainty of Combustion Efficiency Measurements in Flares

Jebin Elias (jebin.elias@utah.edu)

Jennifer P. Spinti (jennifer.spinti@utah.edu)

Sean T. Smith (sean.t.smith@utah.edu)

Philip J. Smith (philip.smith@utah.edu)

The University of Utah, Salt Lake City, UT 84112

Jeremy Thornock (jthornock@gmail.com)

Lawrence Livermore National Laboratory, Livermore, CA 94550

Marc Cremer (cremer@reaction-eng.com)

Minmin Zhou (zhou@reaction-eng.com)

Reaction Engineering International, Salt Lake City, UT 84047

1 Abstract

We describe the continuing development of a Bayesian machine learning methodology for quantifying the uncertainty in downstream combustion efficiency (CE) in ground flares. Our methodology utilizes both experimental measurements and data from multi-physics simulations to produce probabilistic predictions of CE with quantified uncertainty distributions. The strategy outlined in this paper of learning from both experiments and science-based models allows us to make model predictions at conditions other than those where experimental data were collected and for variables that were not measured. Additionally, our strategy can be extended, with necessary adjustments, to any type of flares at any operating condition.

We have applied this methodology to a specific case study - the John Zink SKEC steam-assisted flare at high turndown. The data used for this work were collected at the John Zink Flare Facility as part of Marathon Petroleum Company's Flare Consent Decree¹. The high turndown scenario we chose, the SN1 test suite, is particularly compelling as ground flares typically operate in this standby configuration for a significant portion of their operating life, only to be fully utilized under process upset scenarios or emergencies. The rapid decline of the measured CE in over-assist scenarios during the SN1 tests calls for better understanding of how steam assist affects not only the measured CE but the true (overall) CE at all wind conditions.

In previous AFRC papers^{2,3}, we presented the fundamentals of our Bayesian machine learning methodology using the SN1 test data. We define a parameter set X that we will learn about in the analysis and which affects the quantity of interest, the CE as measured by a Passive Fourier Transform Infrared (PFTIR) spectrometer. While X may include uncertain model and/or scenario parameters, for this case study, X includes only scenario parameters and latent effects (due to physics that are not accounted for in the simulation model nor in the instrument models). We apply Bayes' law to compute a multi-dimensional, joint probability density function that represents the uncertainty and the correlation among the parameters in X having learned from the measured data and the science-based models. We then feed these "validated" parameter values forward through the model to produce posterior predictions of PFTIR measurements of CE with quantified uncertainty distributions that are consistent with the observations.

In the present work, we updated the design of experiments for the surrogate models and ran the corresponding suite of simulations. We re-defined the instrument model used to extract data from the simulations to better follow the experimental measurement specifications. We included the three sets of replicate data for each test condition as a separate experiment and included all three sets in the analysis. Finally, we improved the robustness of the surrogate models by systematic tests and optimization. Our posterior predictives from this analysis show the uncertainty in the CE as measured by the PFTIR.

2 Introduction

Ground flares typically operate in a high-turndown (low fuel flow rate), standby configuration for a significant portion their operating life, being fully utilized only under process upset scenarios or emergencies. Combustion efficiency (CE), a measure of the amount of carbon in the fuel being converted to carbon dioxide, is the quantity of interest (QOI) for such systems. A higher CE results in a lesser amount of unburnt hydrocarbons released into the atmosphere. The actual/overall CE of a flare in operation ($CE_{overall}$) can be affected by several factors to varying degree including the upstream processes, the controlling mechanisms, and/or the prevailing environmental conditions and their influence on the combustion process. Non-intrusive, remote measurement of flare CE at a point or along a line-of-sight or in a plane/volume is not a measurement of $CE_{overall}$ but rather an approximation to it. Such measurements have associated errors that are influenced by the same factors that affect $CE_{overall}$ along with errors that stem from the challenges associated with the consistent usage of the instrument and with the implementation of complex instrument models for converting what was actually measured (e.g., infrared spectra) to CE^{1,4}. More often than not, these errors are not easily identified nor quantified.

For our specific application - the John Zink steam-assisted SKEC flare at high turndown (SN1 data set) - CE was measured using a Passive Fourier Transform Infrared (PFTIR) spectrometer (CE_{PFTIR}). The data were collected at the John Zink Flare Facility as part of Marathon Petroleum Company's Flare Consent Decree (as recorded August 30, 2012) and reported by Clean Air Engineering¹. For PFTIR measurements, CE_{PFTIR} is defined as

$$CE_{PFTIR} = \eta = \frac{\phi_{CO_2}}{\phi_{CO_2} + \phi_{CO} + \phi_{HC}} \quad (1)$$

where ϕ_i is the integrated concentration of each species ($ppm \cdot m$) along a line of sight through the downstream, post-combustion plume.

In this paper, we extend the use of a data-driven, model-based, probabilistic framework that uses the principles of Bayesian inference to quantify the uncertainty associated with CE_{PFTIR} measurements in the SN1 flare tests⁵. The strategy outlined in this paper of learning from both experiments and science-based models allows us to quantify measurement uncertainty and to make model predictions at conditions other than those where experimental data were collected and for variables that were not measured. This Bayesian machine-learning strategy can be extended to any type of flare at any operating condition.

We apply Bayes' law to solve the inverse problem, a statistical method for describing the relationship among the set of uncertain input/controlling parameters X we wish to learn about given some form of observation or evidence of the QOIs (Y)⁶. Mathematically, Bayes' law is defined as

$$p(X|Y) \propto p(X)p(Y|X). \quad (2)$$

where $p(\cdot)$ is a probability distribution.

To solve the inverse problem, the posterior distribution of X given the observed data ($p(X|Y)$), we require priors, $p(X)$, for all X and a likelihood function, $p(Y|X)$. The priors

are distributions that describe the current state of knowledge of a parameter set X , which may include uncertain model and/or scenario parameters and a parameter that accounts for latent effects (physics that are unaccounted for in the simulation and/or instrument models).

The likelihood, $p(Y|X)$, describes the probability of observing the measured data (Y) given a specific parameter set X . The likelihood combines the discrepancy/defect between the science-based model data and the measured variables ($Y_{\text{expt}} - Y_{\text{model}}$) with a model (typically a normal contribution) for the latent effects on the measured variables as shown in Eq. 3.

$$p(Y|X) = \frac{1}{\sigma\sqrt{2\pi}} e^{-\frac{1}{2}\left[\frac{Y_{\text{expt}} - Y_{\text{model}}}{\sigma}\right]^2} \quad (3)$$

where σ , the variance in the QOI, can be further decomposed as described in Section 3.5.

The posterior distribution, $p(X|Y)$, is a multi-dimensional, joint probability density function (PDF) that describes the correlation among the parameters in the set X . It represents the updated state of knowledge of X having learned from both the measured data as well as the science-based model calculations. These “validated” parameter values are then fed forward through the model to produce posterior predictions of CE_{PFTIR} with quantified uncertainty distributions that are consistent with the observations.

3 Bayesian Machine Learning Applied to SKEC Flare

The application of Bayes’ law to the SN1 suite of the SKEC flare test series requires that we complete the following steps:

- Identify and examine the set of test data. Isolate the QOI and study the parameters that influence the QOI, their trends and corresponding operating ranges.
- Define a set of uncertain parameters X to learn about and create a design of experiments (DOE) in the range of X .
- Identify a science-based model for simulating the flare, set up the simulation with the appropriate geometry/inputs/model parameters, and execute the DOE.
- Define an instrument model for computing the QOI from simulation outputs and then use the instrument model to compute the QOI for all simulations in the DOE.
- Create a surrogate model for the QOI as a function of X using the data from the instrument model.
- Assign prior distributions to X , define the likelihood, including the uncertainty σ , Eq. 3, and compute the joint PDF for X using Bayes’ law.
- Compute posterior predictives of the QOI for each measurement point in the data set and compare with the values measured experimentally.

3.1 SN1 Experimental Data

The objective of the SN1 test suite with the steam-assisted SKEC flare¹ was to understand the influence of steam assist on $CE_{overall}$ as approximated by measurements of CE_{PFTIR} and to define an operating envelope for the flare design that (1) sustains a continuous flame at high turndown ratios with the least amount of visible smoke and (2) maintains a $CE_{overall}$ above the legal limits^{4,7}. If the assist stream flow rate is too low, a state called under-assist, excessive visible smoke and particulate pollution result. On the other hand, over-assisting reduces $CE_{overall}$.

For the SN1 tests, three flare tips were located equally spaced along a line. The test data consists of three replicates of six steam flow rates (18 test conditions) resulting in a set of six different conditions for the net heating value of the combustion zone, NHV_{cz} . Tulsa natural gas was the prime flaring fuel used in all of the tests, and the fuel exit velocity at each flare tip was kept relatively constant at 4 ft/s, the lowest possible flow rate to sustain a flame without any flame lift-off for any assist condition as determined *a-priori*. The assist medium, steam, was injected through ports around the fuel inlet, promoting turbulent mixing and entrainment while also reducing the visible smoke. The steam mass flow rate was throttled to create different scenarios of NHV_{cz} ranging from ~ 300 BTU/scf (cooling-steam rate) to ~ 50 BTU/scf (over-assist). The CE_{PFTIR} measurement was made downstream of the three flare tips. Figure 1 illustrates the impact of NHV_{cz} on measured values of CE_{PFTIR} . The trend curve, based on the mean CE_{PFTIR} measurement for each test condition, shows the decline in CE with decreasing NHV_{cz} , especially below NHV_{cz} of 100 BTU/scf.

Each of these 18 test conditions was run for approximately 20 minutes with data recorded every minute. The data set includes fuel and steam flow rates, fuel composition, steam thermodynamic data, wind speed, wind direction, and the QOI, CE_{PFTIR} . The wind speed data at different assist conditions are plotted in Fig. 2. Information at time scales smaller than a minute is unavailable. Also, it is not clear whether any averaging operation was performed on the wind condition measurements. Subjective information such as data related to visible smoke production was also not available.

The CE_{PFTIR} data were collected using two PFTIR devices located approximately 180° from each other in order to have a good view of the flare plume for all possible wind directions¹; see Fig. 3 for a schematic showing the general position of the PFTIR devices relative to the flare. A good view is one that passes nearly perpendicularly through the downstream flare plume. Each device was operated by a technician actively pointing the device's field of view at a location approximately two flame lengths downstream of the flare tip, in the general direction of the flame propagation.

Although it was uncertain where the wind information was collected relative to the flare stacks, careful examination of the SN1 test conditions showed that the wind conditions (wind speed and direction) varied significantly over the 20-minute span of any given test and between tests; see Figs. 2 and 3. As a result, the shape, size, and direction of the flame could have changed quite dramatically within a short period of time, requiring manual

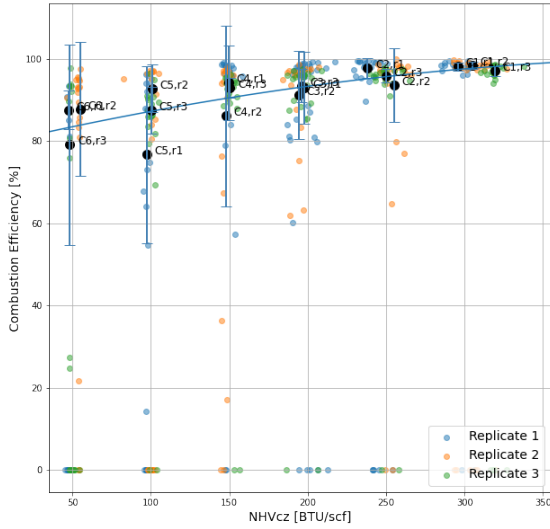


Fig. 1. Declining trend of CE_{PFTIR} values as NHV_{cz} decreases. The dot represents the mean and the error bars represent the range of reported CE_{PFTIR} values for each test condition.

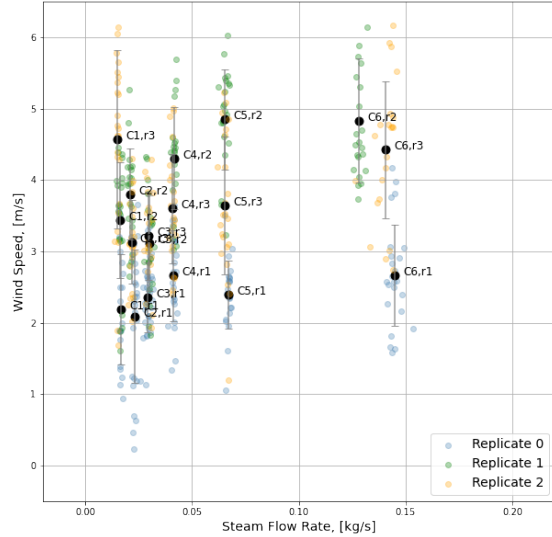


Fig. 2. Recorded minute-by-minute wind speed at different steam mass flow rate conditions for SN1 test suite¹. The error bars show the deviation of wind speed measurements against the corresponding replicate averages.

adjustment of the PFTIR to follow the flame. Such manual adjustment resulted in null records in the minute-by-minute CE_{PFTIR} data.

There are a significant number of null records at the beginning of each 20-minute window of the experimental runs. This is a point where the change in steam flow rates altered the flame shape/length, forcing a re-adjustment of the PFTIR devices. We hence rejected all null records in our evaluation.

There are also zero entries for CE_{PFTIR} at most of the test conditions as noted by the cluster of data points at zero CE in Fig. 1; the over-assist scenarios recorded a relatively higher number of zero measurements. These values are not necessarily *wrong* and contain information about the flare system that should not be ignored. We attribute these zero values to the fact that the CE_{PFTIR} measurements are highly sen-

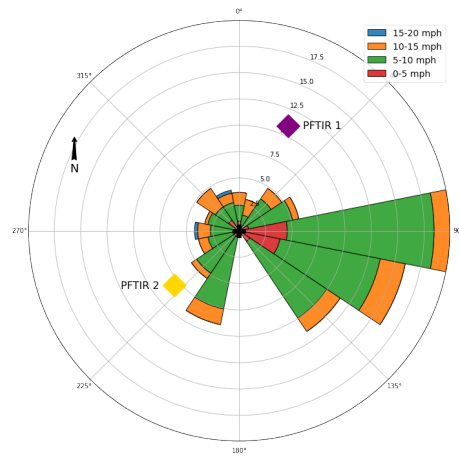


Fig. 3. Frequency plot of wind direction during SN1 experiments. The plot is colored by wind speed. Overlay shows schematic of the PFTIR (purple and yellow diamonds) placement relative to the flare stack (black cross, center).

sitive to the relative position of the PFTIR to the flares and to the location downstream of the flares at which the PFTIR is aimed. Both of these factors determine what is captured in the field of view of the device and hence the infrared spectra collected by the objective lens. In addition, the spectra collected by the PFTIR are integrated/averaged over time to improve resolution and thus isolate spectral information. This averaging smooths out the flame fluttering and puffing effects seen in Figs. 4[b] and 5[b] and may contribute to the measurement of zero values. We include all measured zero values in our analysis.

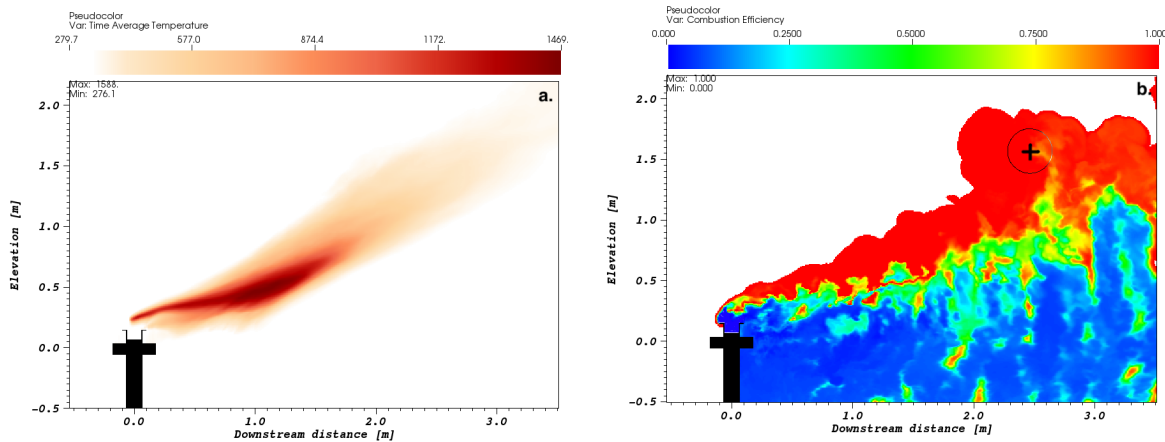


Fig. 4. Simulation results for run 1, replicate 1 (see Table A.1-1 in the Clean Air report¹): [a] Time-averaged temperature field showing long and rising flame with almost no combustion occurring below the flare tip. [b] Instantaneous CE field showing fuel stripping below the horizontal line from the flare tip that results in decreased local CE.

To illustrate how CE_{PFTIR} can be different from $CE_{overall}$, consider a test condition with a large flame (high $NHVCZ$) as shown in Fig. 4. In these simulation results, the location two flame lengths from the flare tip, as identified by the averaged temperature field, is indicated with the crosshair in Fig. 4[b] with the PFTIR field of view at that location approximated by the circle. Fuel stripping occurs near the flare tip as the wind shear carries the fuel stream away from the buoyancy-driven reaction zone. These fuel pockets never get ignited, resulting in degradation of local CE as shown in Fig. 4 [b]. With the visible flame rising up and away and the PFTIR pointed in the general direction of the circle, CE_{PFTIR} would be high relative to the true CE, $CE_{overall}$, as the significant amount of fuel stripping would be unaccounted for in the measurement. However, if the PFTIR were pointed in the direction of the fuel stripping region, an average CE value in the range of 0%-50% would be measured.

In contrast, in over-assist scenarios (see Fig. 5), the steam exiting the injection ports around the fuel inlet effectively shrouds the momentum-driven flame in the combustion zone. The products of incomplete combustion rising from the reaction zone encounter fast-moving steam and are transported away from the high-temperature zone due to the local turbulent intensity and mixing. For a human operator tracking the visible flame, the

flame appears short. In these types of flames, fuel stripping occurs around the flare tip as the steam injection reduces the temperature below the lower flammability limit for the mixture, reducing the reaction rate to zero. Partial combustion also results from the relative velocities of the combustion products and the steam creating a zone of partially oxidised fuel at the center with nearly complete combustion at the periphery (see Fig. 5[b]). These combined effects produce a low CE_{PFTIR} measurement in most of the region downstream of the plume. However, a high CE_{PFTIR} value would be recorded if the PFTIR were aimed at a location on the periphery of the plume.

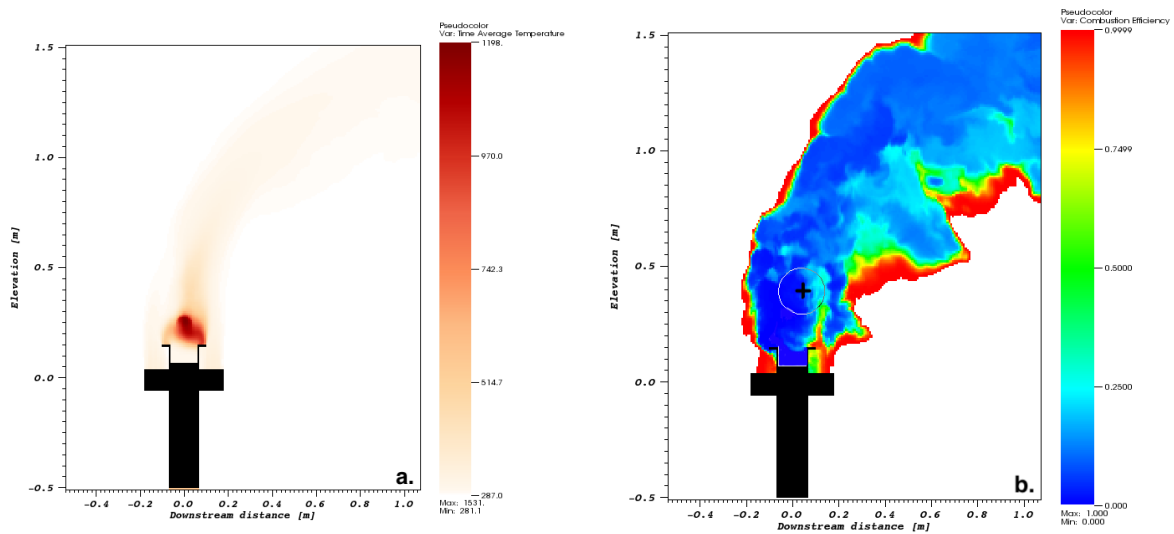


Fig. 5. Simulation results for run 6, replicate 1 (see Table A.1-1 in the Clean Air report¹): [a] Time-averaged temperature profile showing how over-assisting results in a short flame. The flame appears to be contained within a tent above the flare tip. [b] Peripheral region of the rising plume reaches nearly complete combustion while the interior region has low CE values.

The target region for measuring CE in the downstream plume is hence of great significance. However, it is not clear from the description of the process how the field of view of the PFTIR was positioned relative to the three-flare setup. For the higher assist-rate scenarios where the flame is short, it may be difficult to aim consistently at a location two flame lengths from all three flare tips. At lower assist rates, these concerns are somewhat mitigated by the fact that the combustion products from the three flare tips interact further downstream, resulting in a plume that represents the contributions from all three flare tips.

The PFTIR technology generates integrated species concentration values along its line of sight for the species shown in Eq. 1. These values are based on the intensity and frequency of the infrared emission spectrum of each species in the flare plume. An instrument model is used by the operator of the PFTIR to convert the measured signal to a CE_{PFTIR} measurement. This model includes many assumptions and parameters as partially outlined in Appendix A of the Clean Air report¹. There is insufficient information in the report to reconstruct the instrument model used to generate CE_{PFTIR} . Additionally, the environ-

mental effects on the mixing, combustion and diffusion of the flame were not measured nor characterized completely. These factors also influence the recorded data. Hence, the reported CE_{PFTIR} values may have errors from various sources that are not accounted for or are simply too hard to isolate. Nevertheless, by applying Bayesian machine learning to the SN1 test suite, we can quantify the uncertainty in the CE_{PFTIR} measurements.

3.2 Design of Experiments and LES Simulations

We obtained model data for the Bayes' analysis using our multi-phase, computational fluid dynamics code, Arches. Arches is a massively parallel, large eddy simulation (LES) combustion simulator that solves mass, momentum, energy (including radiative energy) and scalar transport equations for single and multi-phase combustion applications. With Arches, we can resolve a wide range of timescales, capturing time-dependent and spatial information for the system of interest. We used the Rate Controlled Constrained Equilibrium combustion model^{8,9} for this study. With this model, we resolved a global combustion rate that constrains a chemical equilibrium assumption, allowing for combustion quenching that is crucial for computing CE. We closed the transport equation set with a dynamic LES turbulence closure that utilizes local turbulent information. We generated the geometric details of the SKEC flare tip using photos, online public information, and flow area information reported with the PFTIR data.

For flares, both $CE_{Overall}$ and CE_{PFTIR} may be functions of many influencing parameters including fuel flow rate, fuel composition, assist stream flow rate, wind conditions, and other scenario parameters. The flare simulations introduce uncertain model parameters that also influence both QOIs. Before performing a suite of simulations, we must first define the subset of parameters that we wish to learn about and the parameter space that we will explore. The instrument models used to obtain CE_{PFTIR} from both the experiments and the simulations require additional parameters which will be discussed separately in Sections 3.3 and 3.4.

We chose to focus only on scenario parameters for this analysis as they tend to dominate downstream CE of flares. For example, Fig. 1 shows the effect of steam feed rate (inversely proportional to NHV_{CZ}) on CE_{PFTIR} . Our parameter set includes:

- Mean steam feed rate, \bar{m}_{steam}
- Mean crosswind speed, \bar{u}_{wind}
- Mean crosswind direction, $\bar{\theta}_{wind}$

In addition to learning about the uncertainty of each of these measured parameters ($\sigma_{\bar{m}_{steam}}$, $\sigma_{\bar{u}_{wind}}$, $\sigma_{\bar{\theta}_{wind}}$), we will learn about the uncertainty of CE_{PFTIR} in the analysis that follows.

We then created a two-dimensional design space for the simulations based on our parameter set. Our design space in the \bar{u}_{wind} dimension spanned all of the measured wind conditions in the SN1 test suite, 0 m/s to 8 m/s (17.9 mi/h). In the \bar{m}_{steam} dimension, the highest recorded steam flow rate was 0.15 kg/s (1216 lb/hr). We extended the coverage to 0.2 kg/s. The third dimension, wind direction ($\bar{\theta}_{wind}$), was incorporated into the analysis via

instrument modeling as described in Section 3.3. We used a uniform-distribution Poisson disc sampling technique to cover the two-dimensional (\bar{u}_{wind} and \bar{m}_{steam}) parameter space with the least points while including the locations where measured data was available. The corner locations were placed intentionally to allow for surrogate training to extend to the edges of the design space. Figure 6 shows the design space for the suite of LES simulations performed.

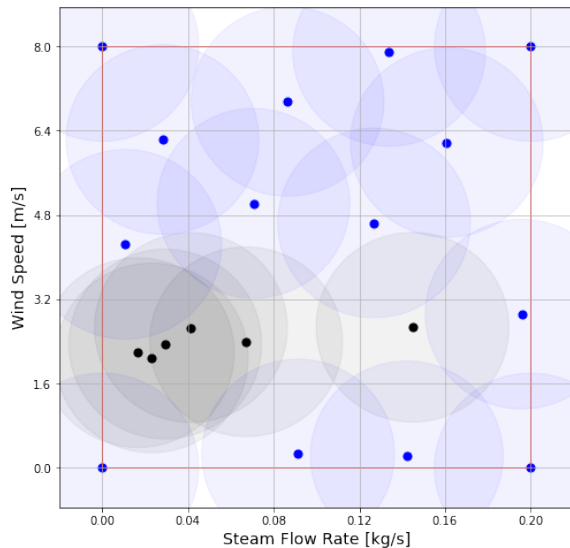


Fig. 6. Design points for the SN1 flare simulation suite. Black locations have experimental measurements, while all locations have LES simulation results associated with them.

We performed an LES simulation for each of the points in the design space with the fuel feed rate held constant. We also assumed a constant fuel composition. While there were three flare tips in the experiment and the CE_{PFTIR} measurement was made downstream of all three plumes, our simulations approximated the three-flare system with a single flare. We ran each simulation for 4-7 days on 800-1500 cores on a local compute cluster at the University of Utah to obtain 10s of simulation time. This time frame was long enough to obtain statistically stationary values of species' concentrations and temperature. We then extracted data from each of the simulations as described in the following section.

3.3 PFTIR Instrument Model for LES Simulations

The LES data must be processed in a way that best replicates the PFTIR device. We developed an instrument model to represent a simplified PFTIR that processes LES data to arrive at an estimation for CE_{PFTIR} .

As described earlier, two PFTIRs, placed northeast and southwest of the flare stack respectively¹, were used in the SN1 tests (see Fig. 3 for an approximate representation of the PFTIR locations) to ensure that at least one had a good field of view as per the guidelines set for the instrument usage. The ideal configuration is to place the PFTIR such

that its line of sight is perpendicular to the direction of the flame plume. However, due to the fluctuating nature of the prevailing wind, it was nearly impossible to enforce this criterion.

The calculation of CE_{PFTIR} using the PFTIR line-of-sight measurement is sensitive to this relative position of the sensing device and the flame plume. The two PFTIRs were placed nearly $40m$ and $60m$ away from the flare stack when viewed from above. In cylindrical coordinates, if we assume the flare stack to be the centre, the two PFTIRs are at different radii on the ground plane. Figure 7[a] shows this coordinate system when viewed from above with the flare represented by the black diamond. Because the flame follows the prevailing wind direction, the position of the PFTIR can be defined as an angle θ relative to the flame. Therefore, to simulate any wind direction, the PFTIR instrument model can be placed at either of the two radial distances and at any angle relative to the flame. In our instrument model, we spanned θ_{wind} space by sampling a collection of points around two circular loci corresponding to the radial distances at which the actual devices were placed. Figure 7[a] shows a selection of ten such sampling locations for clarity.

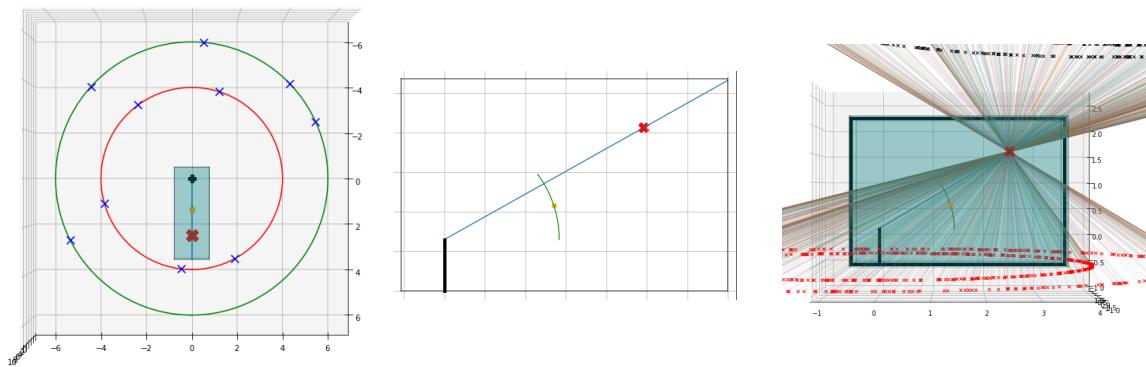


Fig. 7. PFTIR instrument model: [a] PFTIR instrument model positions at two radii (green and red circles) representing loci of all possible locations for the PFTIR instrument model placement, and thereby the corresponding wind directions. Blue crosses on these circles shows a selection of ten such sampling locations. [b] Schematic showing the flare stack (black line), the direction of flame propagation (blue line), the flame tip locii (green arc), and the PFTIR target (red cross). [c] Collection of 1000 positions for PFTIR instrument model distributed around the flare stack at both radii with lines of sight from these points through the target location within the computational domain.

The CE_{PFTIR} measurement is also sensitive to the target location downstream of the flame. As the flame shape and size are dependent on the reaction rate, turbulent mixing, and wind speed/direction among other factors, the location at which the PFTIR is aimed also varies. The visible flame is the envelope of the region where primary combustion occurs; the PFTIRs were pointed approximately two flame lengths away from the flare tip as viewed by the operator. To identify a similar location for the simulation results, we first time-averaged the temperature field and then identified the location of the maximum temperature in the center plane of the flare. Figure 7[b] shows the schematic of the target

location selection. Assuming the wind to be moving from the left, the black line represents the flare stack, the green arc represents the average downstream flame front limit, and the orange dot represents the location of the maximum average temperature. The radial distance from the flare tip to the location of highest temperature was then defined as the average flame length for the case. Temperature gradients at spherical sections further away from the flare stack traced the general direction of flame travel represented by the blue line originating from the flare tip. We then fixed a target location for the PFTIR instrument model that was two flame lengths away from the flare tip along the approximate line of flame propagation, shown as a red cross in the schematic.

Time averaging while measuring a spectral property flattens the instantaneous fluctuations in the actual property. The experimental measurements are time-averaged over one minute. To be consistent in our instrument model, we first time-averaged the scalar fields needed for the model over the last 6s of the 10s simulation window. We sampled 1000 points on the two circles representing the PFTIR locations based on a uniform probability assumption spread equally between the two radial distances to represent possible wind directions and thereby possible locations of the PFTIRs relative to the flare stack. We then extracted line-of-sight data from the time-averaged fields along the line originating from every sampled point to the target location. Every line-of-sight PFTIR ray yields a species concentration trace for carbon dioxide, carbon monoxide and total unburnt hydrocarbons ($i = CO_2, CO, \text{ and } HC$). The integration along the line of sight uses the fuel mixture fraction to weight the contribution of each local species:

$$\phi_i = \frac{\sum_j f_j \phi_j}{\sum_j f_j} \quad (4)$$

where i is the species index, j is the line-of-sight position index, and f is the total fuel mixture fraction, m_{fuel}/m_{total} . The integration also followed an inverse distance weighting in computing the contribution from each point along the line to the integrated quantity as seen in Eq. 5,

$$\Phi_i = \left(\sum_l \frac{\phi_i|_l}{r_l} \right) / \left(\sum_l \frac{1}{r_l} \right) \quad (5)$$

Here, l represents every point along the line and r_l is the distance from the origin to the location. Following this approach, the closest point to the origin of the ray has the highest weight in the integration and the farthest point has the least weight.

3.4 Surrogate Model for Combustion Efficiency

Our Bayesian analysis requires fast function evaluations of CE_{PFTIR} as a function of the parameter set X - \bar{m}_{steam} , \bar{u}_{wind} , and $\bar{\theta}_{wind}$. We created a surrogate model for the QOI, CE_{PFTIR} , using the CE_{PFTIR} data extracted from the suite of simulations in the design space.

We generated the CE_{PFTIR} surrogate model (Y in Bayes' law, Eq. 2) using a Gaussian process regression engine developed *in-house* by co-author Sean Smith. This pythonic package is used for unsupervised learning given prior functions for the parameter set X . The surrogate model can be 'trained' on a set of data and then queried at any location within the parameter space to yield a model prediction for the QOI.

As discussed above, our instrument model is fully described by the following parameters:

- Mean steam feed rate, \bar{m}_{steam} , and mean crosswind speed, \bar{u}_{wind} .
- Relative position of the PFTIR described by :
 - Mean crosswind direction $\bar{\theta}_{wind}$ (also the relative angular position of the PFTIR instrument model).
 - Choice of PFTIR as represented by the radial distance of each position.
- Target location for the PFTIR instrument model.

In the current implementation of our instrument model, we fixed the target location for each case based on the time-averaged temperature field following the heuristic described in Section 3.3. To further reduce the dimensionality of the problem, we separated the experimental and simulation data into two sets based on the radial distance of the PFTIR. Thus, we had two surrogate models, one for each PFTIR, that were functions of three parameters in X - \bar{m}_{steam} , \bar{u}_{wind} , and $\bar{\theta}_{wind}$. Mathematically, it can be summarized as:

$$CE_{PFTIR} = Y_{CE_{IM}}(\bar{m}_{steam}, \bar{u}_{wind}, \bar{\theta}_{wind}) \quad (6)$$

We based the two surrogate models on the Squared Exponential kernel defined using the individual set of optimized hyperparameters. We based the choice of surrogate model on the radial distance from the PFTIR to the flare. We trained the surrogate models on a randomly chosen set of parametric locations that comprised 80% of the CE_{PFTIR} instrument model data. We tested the surrogate models on the remaining 20% of the data by comparing the CE_{PFTIR} predictions from the surrogate model to the values obtained from the instrument model. Figure 8 shows the parity between the surrogate model predictions for both models (green and blue dots) and the corresponding instrument model values. The linear regression score for the correlation is 0.999,

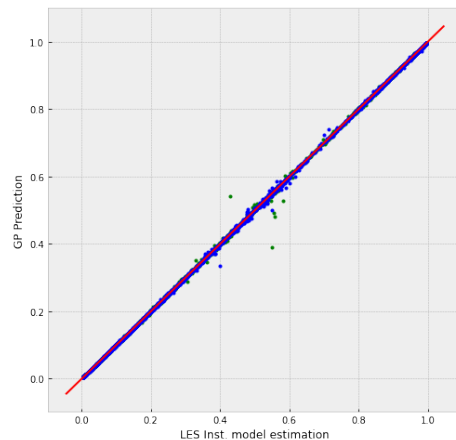


Fig. 8. Predictions of CE_{PFTIR} from the two surrogate models (green and blue dots) compared against the instrument model data set. Red line shows perfect parity.

showing that the surrogate model is consistent with the instrument model values at all locations within the parameter space.

We also evaluated the sensitivity of the surrogate models to different cases in the LES suite to ensure that the response surface of the surrogate model was consistent across the parameter space. We performed this exercise iteratively to optimize the hyperparameters of the Gaussian process by training the surrogate model on different sets of data representing each of the test conditions in the LES simulation suite and then testing the surrogate on the remaining data points. Our goal was to ensure that the predictions from the model followed the same trend and that no case created a bias in the surrogate model predictions. We used a histogram of the predictions on an equally spaced grid spanning the entire parameter space to evaluate the surrogate model at every step. We found that the surrogate model was sensitive to a few of the cases at the edges of the two-dimensional parameter space. We added noise to the kernel to mitigate this issue by preventing the covariance matrix from becoming degenerate.

3.5 Estimating Uncertainty of Combustion Efficiency Measurements

We are now ready to perform a Bayesian analysis to determine the uncertainty in the CE_{PFTIR} measurements. We are learning about the uncertainties in the measured variables, $\sigma_{\bar{m}_{steam}}$, $\sigma_{\bar{u}_{wind}}$, and $\sigma_{\bar{\theta}_{wind}}$, which we term errors-in-variables¹⁰. Additionally, we learn about $\sigma_{CE_{PFTIR}}$, the uncertainty in the measurement due to latent effects.

Bayes' law requires that we define priors for the parameters in X . We choose the priors to be wide and constant. We define the likelihood function for Bayes' law (Eq. 2) as:

$$p(CE_{PFTIR} | \bar{m}_{steam}, \bar{u}_{wind}, \bar{\theta}_{wind}) = \frac{1}{(\sqrt{2\pi}\sigma_t^2)^N} \exp\left(-\frac{1}{2\sigma_t^2} \Sigma [Y_{CE_{exp}} - Y_{CE_{IM}}(X)]^2\right) \quad (7)$$

where $Y_{CE_{IM}}$ is the surrogate model query (Eq. 6) at the location $X = (\bar{m}_{steam}, \bar{u}_{wind}, \bar{\theta}_{wind})$ in parameter space. The total overall uncertainty in the posterior distribution of CE_{PFTIR} is characterized by:

$$\sigma_t^2 = (\sigma_{CE_{PFTIR}})^2 + \left(\frac{dY_{CE_{IM}}}{d\bar{m}_{steam}} * \sigma_{\bar{m}_{steam}}\right)^2 + \left(\frac{dY_{CE_{IM}}}{d\bar{u}_{wind}} * \sigma_{\bar{u}_{wind}}\right)^2 + \left(\frac{dY_{CE_{IM}}}{d\bar{\theta}_{wind}} * \sigma_{\bar{\theta}_{wind}}\right)^2 \quad (8)$$

We employed an optimizer algorithm to locate a local mode in the parameter space that minimizes the discrepancy between the measured CE_{PFTIR} data and $Y_{CE_{IM}}$ from the simulation instrument model. We then used this mode to initiate a Monte-Carlo sampler. We ran a Monte-Carlo simulation of the negative log of the Bayes' equation using 20 threads for 1500 iterations to produce converged distributions of the parameters. We rejected the

first 300 samples to account for burn-in for the sampler, and used the remaining samples to compute the joint posterior distribution of the uncertain parameters. In order for the CE_{PFTIR} values from the surrogate model to be bounded within the limits of 0% and 100% during Monte-Carlo sampling, we transformed the QOI data into a Gaussian space that is essentially unbounded using an inverse error transform function. After computing the posterior predictives, we transformed the results back into real linear space.

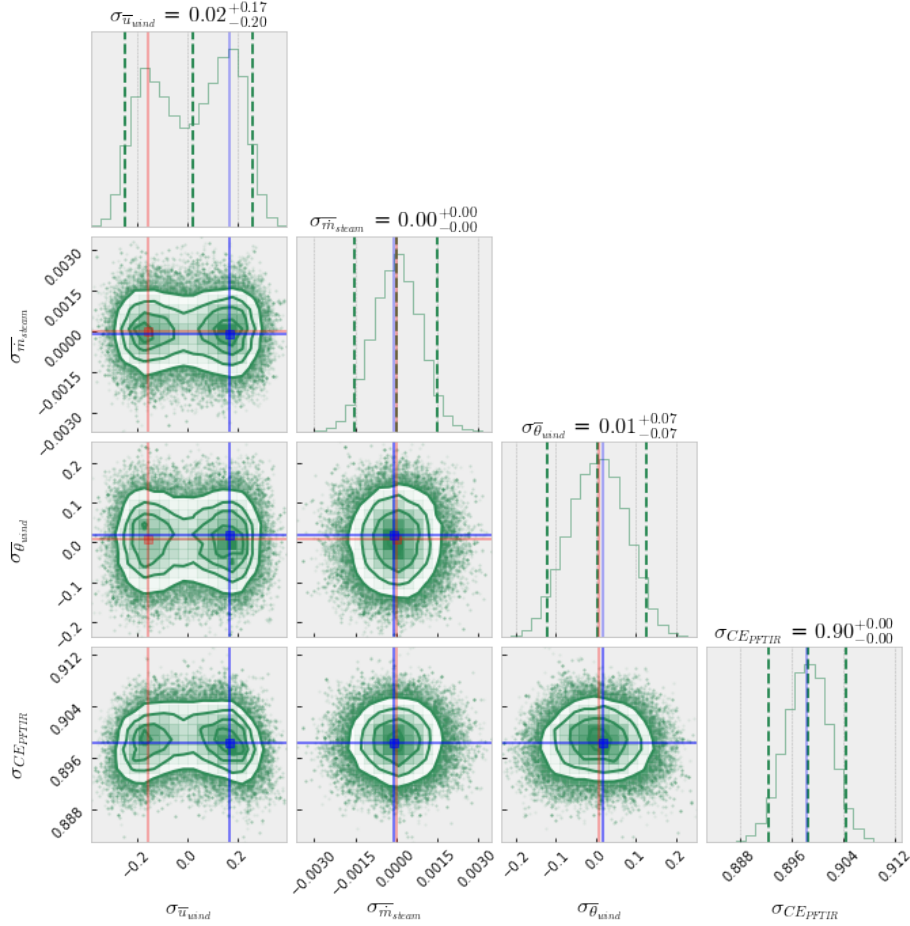


Fig. 9. Joint posterior distribution from Monte Carlo sampling of four parameters ($\sigma_{\bar{m}_{steam}}$, $\sigma_{\bar{u}_{wind}}$, $\sigma_{\bar{\theta}_{wind}}$, and $\sigma_{CE_{PFTIR}}$) for 1500 iterations with 20 threads.

The joint posterior distribution of the parameter set X in Fig. 9 shows the correlation between each pair of the parameters. Careful examination of the uncertainty ranges shows that the overall unaccounted-for errors ($\sigma_{CE_{PFTIR}}$) have a much larger uncertainty than the uncertainties in the measured input variables. Also, none of the parameter pairs show a strong correlation. Marginal posterior distributions shown in the diagonal plots in Fig. 9 show a bimodal trend for the uncertainty in the wind speed measurements while the errors in the wind direction measurements demonstrate a nearly normal distribution with equal spread.

Figure 10 shows the posterior predictives of CE_{PFTIR} having learned from the data. We generated these data at each recorded data point (\bar{m}_{steam} , \bar{u}_{wind} , and $\bar{\theta}_{wind}$) by first sampling N times from the joint posterior distribution shown in Fig. 9. We add the sampled uncertainties to the corresponding value of the recorded data point and feed these modified values forward through the model, Y_{CEIM} . We then add in the sampled uncertainty in CE_{PFTIR} . We repeat this process N times to generate the distribution at each recorded data point shown in the figure. The modes of these predictions (red dots) reflect the most probable prediction with the blue violin plots showing the range of the predictions. The decline in CE with smaller NHV_{cz} , as recorded by the experiments (see Fig. 1), is reflected in the posterior predictives. Our methodology generates predictions that are consistent with the experimental measurements while also quantifying the large uncertainty associated with these types of measurements.

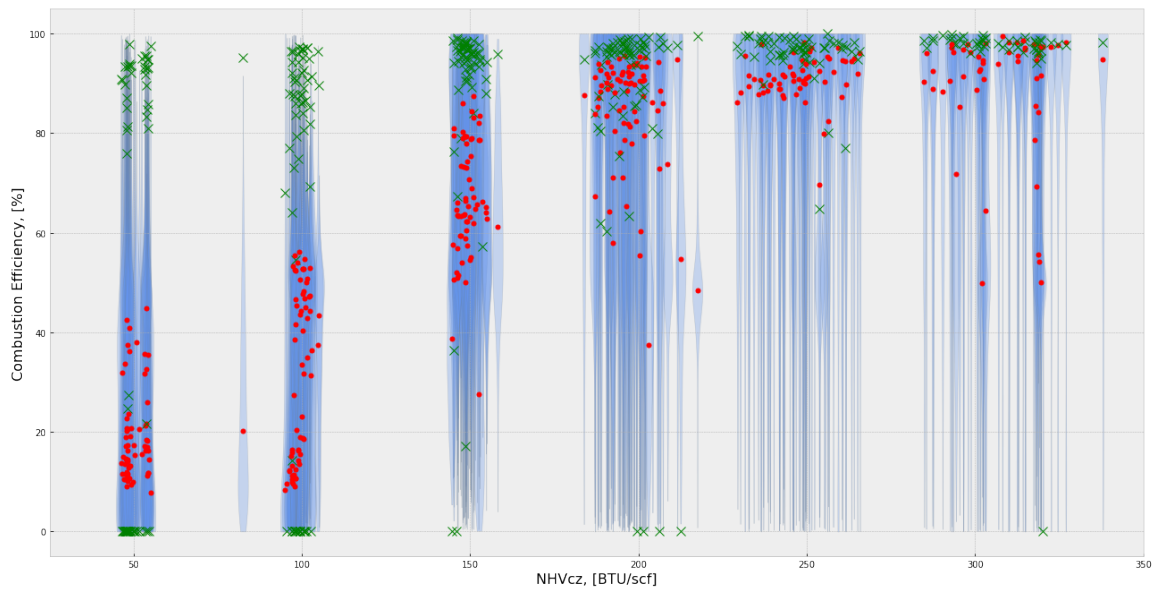


Fig. 10. Distribution of posterior predictives of CE_{PFTIR} (red dot is mode, blue lines are uncertainty ranges) plotted with the experimental measurements (green cross) against NHV_{cz} .

The distribution of the CE_{PFTIR} posterior predictives at different NHV_{cz} values is presented in the form of violin plots in Fig. 11. The left half of the split plot at each NHV_{cz} location shows the distribution of the CE_{PFTIR} predictives due to the latent effects alone. This plot assumes that the errors in the measurements of the parameter set X are zero, and therefore the uncertainty in the predictions are due to errors from sources that are unaccounted for in the analysis. The right half of the split plot shows the distribution of the CE_{PFTIR} posterior predictives accounting for the uncertainty distribution of the measured parameters in X (Eq. 8) but discounting the uncertainties induced due to latent effects. Evaluating the two halves together shows that the latent effects are the largest contributor to the CE_{PFTIR} measurement uncertainty and that the uncertainties in the measurement of wind speed, wind direction and steam flow rate combined together produce a much smaller

uncertainty spread. The trend curve shown in blue passes through the mode (red cross) of the posterior predictives at each NHV_{cz} location considering the uncertainty in all of the parameters in X (due to latent effects as well as measurement errors). The violet highlighted region shows the highest CE ranges of 98%-100%. For comparison, we computed the average value of CE_{PFTIR} at each test condition (three replicates for each of six NHV_{cz} values) from approximately 20 minutes of data recorded every minute. These values are shown as black diamonds at each NHV_{cz} location (three replicates per location). The larger blue diamond represents the average of the three replicate averages. The spread of the mean values of the CE_{PFTIR} measurements from the replicates is quite large for higher assist rates (lower NHV_{cz}) and decreases as the steam flow rates move closer to under-assist conditions.

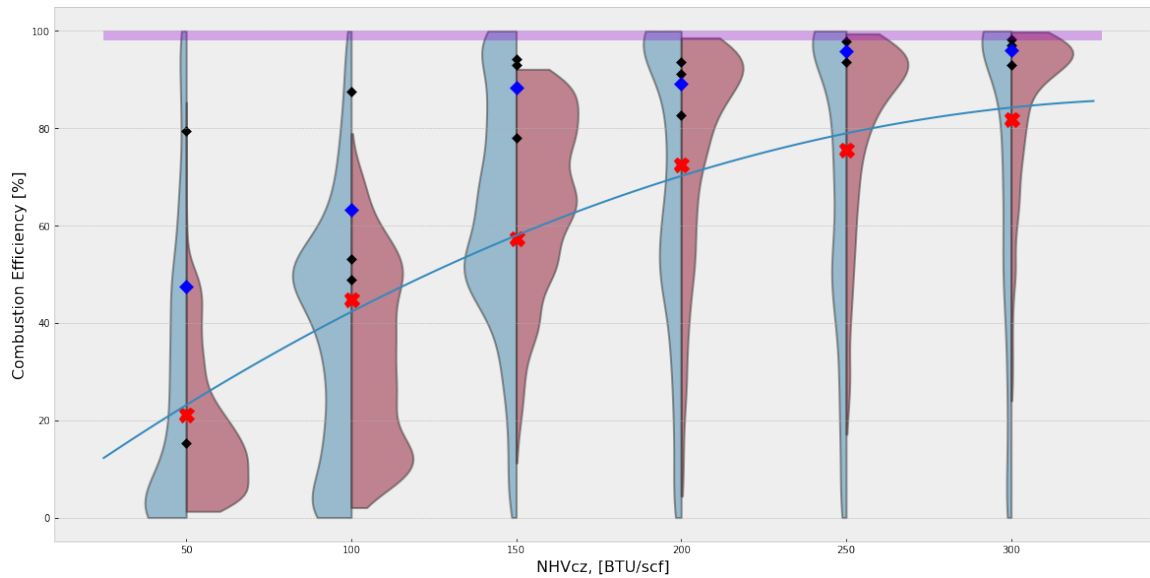


Fig. 11. Split violin plot showing the overall uncertainty in the CE_{PFTIR} predictions due to unaccounted-for errors on the left, with that due to errors in measured inputs on the right. The trend curve shows the mode of the posterior predictions of CE_{PFTIR} considering all the uncertainties (errors from measured parameters and from unaccounted-for sources). Experimental measurements are plotted as averages of each replicate of the six scenarios (black dots at each NHV_{cz}). Trend of the experimental measurements of CE_{PFTIR} is shown as blue diamonds. CE range of 98%-100% is highlighted in violet.

4 Conclusions

We applied the method of Bayesian machine learning to the SN1 test data, a series of runs conducted on the John Zink steam-assisted SKEC flare¹. Our objective was to quantify the uncertainties in the PFTIR-measured CE, CE_{PFTIR} , at various assist rates by identifying

and categorizing the sources of these uncertainties, thereby generating confidence intervals that help define the operating envelope of the flare.

By careful evaluation, we identified a set of parameters that directly influence the CE_{PFTIR} test data spanning six $NHVCZ$ conditions. From this set, we selected two parameters, wind speed and steam flow rate, and performed a suite of 20 LES computations of the SKEC flare to cover this two-dimensional parameter space. We defined an instrument model that was consistent with the experimental PFTIR data collection process and extracted line-of-sight scalar data from the LES simulation suite using the model. We used this CE_{PFTIR} data from the simulations to train a Gaussian process regressor (surrogate model). Using this surrogate model and the experimental measurements, we computed the joint posterior distribution of the uncertain parameters. We then computed the posterior predictive for CE_{PFTIR} at multiple $NHVCZ$ locations by sampling from the joint posterior distribution and feeding the sampled parameter values forward through the model.

We identified the effect of errors in steam flow rate, wind speed, and wind direction on the CE_{PFTIR} measurements. However, the uncertainty ranges of the predictions indicate significant contributions to the overall errors from sources that were not considered in this analysis. The CE_{PFTIR} measurements for any assist rate scenario are dependent on the local environmental conditions, which influence the choice of the PFTIR sampling location in the flare plume; this target location uncertainty contributes to the overall error. Human-induced errors on the PFTIR readings along with the layers of instrument modeling within the PFTIR readings also contribute to the overall uncertainty in the measurements.

The findings from this study can be extended to predict an overall/actual CE ($CE_{overall}$) with uncertainty, a quantity that consolidates the uncertainties in the measurements and in the combustion physics parameters.

Acknowledgments/Disclaimer

This material is based upon work supported by the U.S. Department of Energy, Office of Science, under Award Number DE-SC0017039. The authors wish to thank Dan Pearson and Scott Evans at Clean Air Engineering for answering our many questions related to the flare test data.

This paper was prepared as an account of work sponsored by an agency of the United States Government. Neither the United States Government nor any agency thereof, nor any of their employees, makes any warranty, express or implied, or assumes any legal liability or responsibility for the accuracy, completeness, or usefulness of any information, apparatus, product, or process disclosed, or represents that its use would not infringe privately owned rights. Reference herein to any specific commercial product, process, or service by trade name, trademark, manufacturer, or otherwise does not necessarily constitute or imply its endorsement, recommendation, or favoring by the United States Government or any agency thereof. The views and opinions of authors expressed herein do not necessarily state or reflect those of the United States Government or any agency thereof.

References

- [1] Clean Air Engineering. Performance test of steam-assisted and pressure assisted ground flare burners with passive ftir – garyville. Technical report, Marathon Petroleum Company, LP, 2013. Project No: 12082.
- [2] Jeremy N. Thornock, Mikhael Hradisky, Minmin Zhou, and Marc Cremer. Data informed multipoint ground flare evaluation using measurement and theory. *American Flame Research Committee*, 2019.
- [3] Marc Cremer, Minmin Zhou, Dave Wang, and Jeremy N. Thornock. Hardening of arches for commercial simulation of industrial flares: A program update. *American Flame Research Committee*, 2020.
- [4] M McDaniel. Flare efficiency study. Technical report, United States Environmental Protection Agency: Washington DC.
- [5] Marc Cremer, Minmin Zhou, and Dave Wang. Hardening of Arches for Commercial Simulation of Industrial Flares: A Program Update. Technical report, AFRC Virtual Industrial Combustion Symposium, 2020. October 19-21.
- [6] A Gelman, J B Carlin, H S Stern, D B Dunson, A Vehtari, and D B Rubin. *Bayesian Data Analysis, Third Edition*. Chapman & Hall/CRC Texts in Statistical Science. Taylor & Francis, 2013.
- [7] United States Government Code of Federal Regulations-Standards of Performance for New Stationary Sources, General Control Device and Work Practice Requirements.
- [8] James C. Keck. Rate-controlled constrained-equilibrium theory of chemical reactions in complex systems. *Progress in Energy and Combustion Science*, 16(2):125 – 154, 1990. ISSN 0360-1285.
- [9] James C. Keck and David Gillespie. Rate-controlled partial-equilibrium method for treating reacting gas mixtures. *Combustion and Flame*, 17(2):237 – 241, 1971. ISSN 0010-2180.
- [10] R.J. Carroll, D. Ruppert, L.A. Stefanski, and C.M. Crainiceanu. *Measurement Error in Nonlinear Models: A Modern Perspective, Second Edition*. Chapman & Hall/CRC Monographs on Statistics & Applied Probability. CRC Press, 2006.